Multi-resolution graph-based analysis of histopathological whole slide images: Application to mitotic cell extraction and visualization

Vincent Roullier [a,*], Olivier Lézoray [a], Vinh-Thong Ta [b], Abderrahim Elmoataz [a]

[a] Université de Caen Basse-Normandie, GREYC UMR 6072 CNRS – Image Team, 6, Boulevard Maréchal Juin, F-14050 Caen, France
[b] LaBRI (Université de Bordeaux, CNRS, IPB), 351 cours de la Libération, F-33405 Talence Cedex, France

ARTICLE INFO

ABSTRACT

In this paper, we present a graph-based multi-resolution approach for mitosis extraction in breast cancer histological whole slide images. The proposed segmentation uses a multi-resolution approach which reproduces the slide examination done by a pathologist. Each resolution level is analyzed with a focus of attention resulting from a coarser resolution level analysis. At each resolution level, a spatial refinement by label regularization is performed to obtain more accurate segmentation around boundaries. The proposed segmentation is fully unsupervised by using domain specific knowledge.

© 2011 Elsevier Ltd. All rights reserved.

1. Introduction

1.1. Clinical context

Breast cancer is the second leading cause of cancer death for women. Its incidence increases substantially and continuously while the mortality rate remains high despite earlier detection and advances in therapeutic care. The identification and the use of reliable prognostic and therapeutic markers is a major challenge for decision-making regarding therapy. Proliferation has been shown to be the strongest prognostic and predictive factor in breast carcinoma, especially in patients lacking lymph node metastases [1]. This parameter is daily taken into account by the pathologist for establishing the histopathological grading of breast carcinomas, using enumeration of mitotic figures, through the lens of the microscope. The recent use of immunohistochemical staining of mitosis is able to facilitate their detection [2]. Nevertheless, the visual counting method remains subjective [3] and leads to reproducibility problems due to the frequent heterogeneity of breast tumors [4].

The recently introduced microscopical scanners allow recording large images of the whole histological slides and offer the prospect of fully automated quantification for a better standardization of proliferation rate appraisal. If the advent of such digital whole slide scanners has triggered a revolution in histological imaging, the processing and the analysis of breast cancer high-resolution histopathological images is a very challenging task [5,6]. First, the produced images are relatively huge and their processing requires computationally efficient tools. Second, the biological variability of the objects of interest makes their extraction difficult. As a consequence, few works in literature have considered the processing of whole slide images and most of these works rely only on machine learning techniques [7–10].

1.2. Our approach

In this work, we present a graph-based multi-resolution segmentation strategy for histological breast cancer whole slide images. The proposed strategy is based on a top-down approach that mimics the pathologist interpretation under the microscope as a focus of attention. The proposed segmentation performs an unsupervised clustering at each resolution level (driven by domain specific knowledge) and refines the associated segmentation in specific areas as the resolution increases. The whole strategy is based on a graph formalism that enables to perform the segmentation adaptation at each resolution. Mitosis extraction is performed at the last resolution. Finally, visualization tools are proposed to pathologists for establishing the mitotic count.

1.3. Paper description

The paper is organized as follows. A description of the considered images is presented in Section 2.1. In this section, we also describe the visual analysis process performed by pathologists to evaluate mitotic figures proliferation and their inherent

---

* Corresponding author. Tel.: +33 677545227.
  E-mail address: vincent.roullier@greyc.ensicaen.fr (V. Roullier).

multi-resolution approach. Our graph-based formulation for image segmentation is presented in Section 3 and its integration into a multi-resolution segmentation strategy is detailed in Section 4. Section 5 presents visualization tools of extracted mitosis. Evaluation is presented in Section 6. Last section concludes.

2. Image description

2.1. Visual grading of histological images

Within the last decade, histological grading has become widely accepted as a powerful indicator of prognosis in breast cancer. The majority of tumor grading systems currently employed for breast cancer combine nuclear grade, tubule formation and mitotic rate. In general, each element is given a score of 1-3 (1 being the best and 3 the worst) and the score of all three components are added together to give the breast cancer grading. The usual breast cancer grading scheme is the Elston–Ellis criterion [11] and is based on three separated scores:

- *Gland (tubule) formation*: one scores the proportion of whole carcinoma that forms acini (1: >75%; 2: 10–75%; 3: <10%).
- *Nuclear pleomorphism*: one scores the nuclear atypia according to size, shape and chromatin pattern (1: none; 2: moderate; 3: pronounced).
- *Mitotic count*: one scores the number of mitotic figures per 10 consecutive high power fields (1: 0–9 mitoses; 2: 10–19 mitoses; 3: > 19 mitoses).

The final grading is obtained by adding the three scores. The total score is in the range 3–9 and the final obtained grading is:

- **Grade 1**: if total score is 3–5.
- **Grade 2**: if total score is 6–7.
- **Grade 3**: if total score is 8–9.

In this work, we are interested in mitosis detection for helping pathologists to establish an accurate mitotic count [12]. Such a process can be greatly facilitated with the use of whole slide images.

2.2. Breast cancer histological whole slide images

Breast cancer tissue samples are sectioned at 5 μm thickness and stained with an immunohistochemical (hematoxylin and eosin) method. A ScanScope CS ^{TM} (Aperio®, San Diego, CA) digital microscopical scanner is then used to digitalize each slice at 20× magnification scale and the resulting digital images are compressed with a quality of 75% following the JPEG compression scheme.

To facilitate the visualization and the processing, scanned samples acquired by the scanner are directly stored as an irregular pyramid where each level of the pyramid is an under resolved version of the highest resolution image (the pyramid base). Fig. 1 presents such a pyramidal structure and the ratio between each resolution levels.

The usual size of a compressed whole slide image is about 100–500 Megabytes after compression. However, the resulting whole slide images are too large in size to be processed or visualized as a whole. Therefore, the whole slide image is tiled by the scanner to ease both its processing and visualization: each resolution level of the pyramid is split into image tiles in a non-overlapping layout.

2.3. Multi-resolution approach

Our approach is based on a top-down process that mimics the pathologist interpretation under the microscope as a focus of attention. Using a focused multi-resolution approach enables to reduce
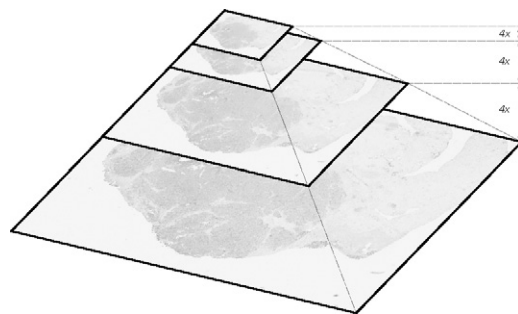

Fig. 1. Example of pyramidal decomposition of a tissue sample scanned by a whole slide image scanner.

the amount of data to be processed [13] similarly as the way as pathologists interpret slide content under a microscope: regions of interest are determined at low resolution while more subtle cellular differentiation are evaluated at high resolution. For the special case of mitotis extraction in breast cancer grading, we can describe in details the analysis of a pathologist as follows:

- Separate tissue and slide background.
- Retain only tissue lesions rather than the normal surrounding tissue.
- In tissue lesions, retain only regions where tumorous cells groups appear rather than regions with stroma and normal glandular acini.
- Extract mitotic figures into the previously retained regions.

Finally, this analysis is performed by the pathologist with an increasing resolution between each of the four steps. Fig. 2 illustrates the complete visual analysis process. To be compliant with the way pathologists examine breast cancer tissue samples, but also to ease their understanding of an automated processing, our approach follows exactly this multi-resolution analysis. This multi-resolution analysis will be based on processing tools that consider an image as a graph leading therefore to a graph-based segmentation. Before describing in depth the multi-resolution segmentation, we provide in next section the key elements of graph-based segmentation as the basis of our multi-resolution approach.

3. Graph-based segmentation

Our strategy for multi-resolution segmentation makes use of regularization on graphs both for image simplification and segmentation as the core algorithms of our multi-resolution approach. We recall in this section some basic definitions on graphs, and we define operators which can be considered as discrete versions of continuous differential operators. We also describe a set of graph-based tools by formulating a discrete regularization framework of data and labels [14,15].

3.1. Preliminaries on graphs

A graph is a structure used to describe a set of objects and the pairwise relationships between those objects. We assume graphs to be undirected, with no self-loops and no multiple edges (see in [16] for details on theses notions). The objects are called *vertices* and a link between two objects is called an *edge*. A *weighted graph* $G = (V, E, w)$ consists in a finite set $V = \{v_1, \ldots, v_N\}$ of N vertices, a set of edges $E \subset V \times V$ and a symmetric weight function $w : E \rightarrow \mathbb{R}^+$ satisfying $w(u, v) = 0$ if (u, v) is not an edge of E. The notation $u \sim v$ is also used to denote two adjacent vertices. In this paper, Gaussian kernels are considered as weight functions with $\sigma = 20$. Let $\mathcal{H}(V)$ be the Hilbert space of real-valued functions defined on the vertices of
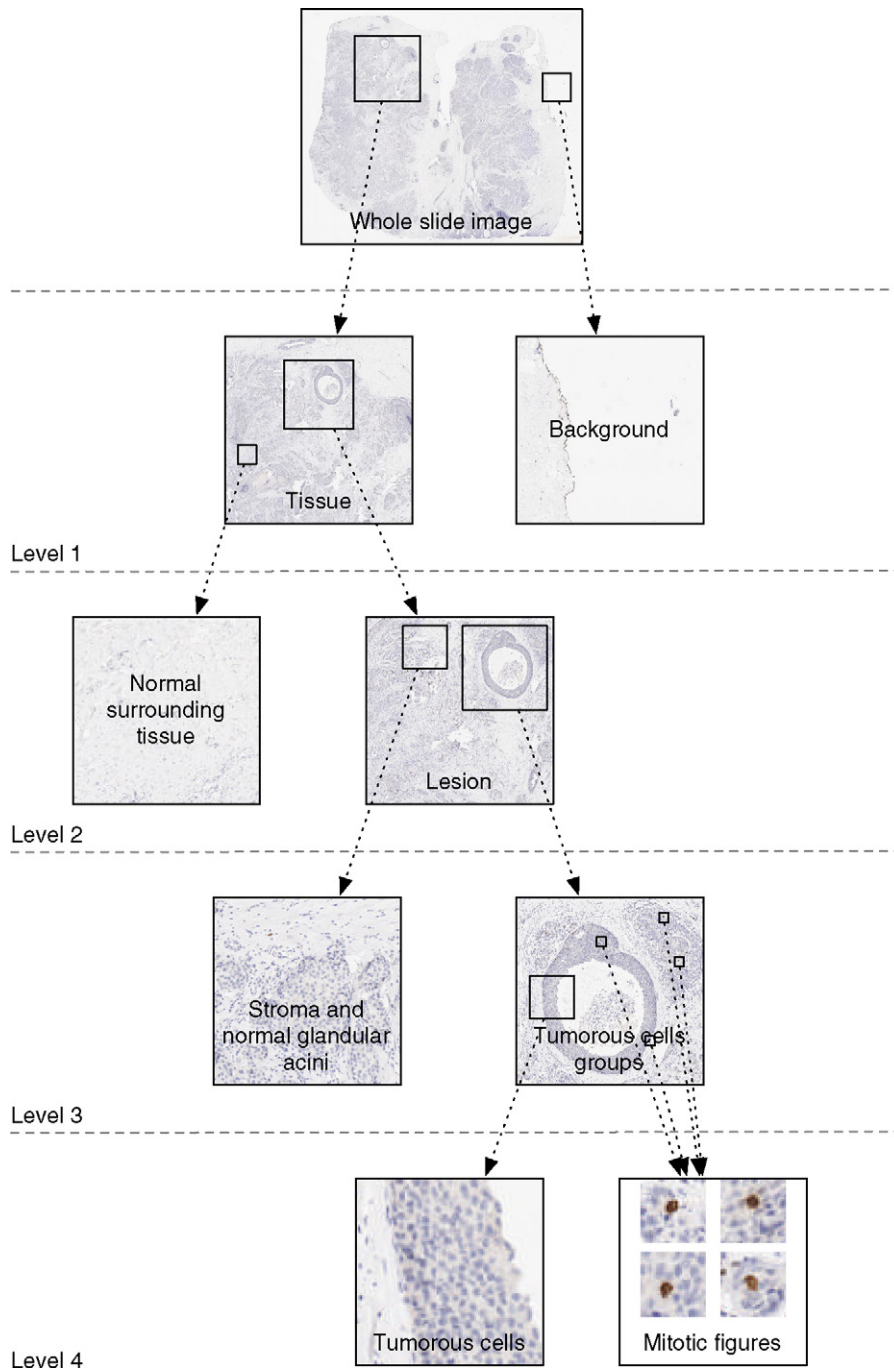
Fig. 2. Visual analysis process performed by a pathologist. Each decision is performed at a higher resolution than the previous one in the decision tree. Level 1: tissue versus background. Level 2: lesion versus normal surrounding tissue. Level 3: tumorous cells groups versus stroma and normal glandular acini. Level 4: tumorous cells versus mitotic figures.

a graph. A function $f : V \to \mathbb{R}$ of $\mathcal{H}(V)$ assigns a real value $f(v)$ to each vertex $v \in V$. Similarly, let $\mathcal{H}(E)$ be the space of real-valued functions defined on the edges of a graph. Graph structures are extremely useful and occur naturally while processing digital images: vertices represent pixels and edges represent 8-adjacency relationships.

3.2. Discrete operators on graphs

Let $G = (V, E, w)$ be a weighted graph, and let $f : V \to \mathbb{R}$ be a function of $\mathcal{H}(V)$. The *difference operator* of f, noted $d : \mathcal{H}(V) \to \mathcal{H}(E)$, is defined on an edge $(u, v) \in E$ by $(df)(u, v) = \sqrt{w(u, v)}(f(v) - f(u))$. The *weighted gradient operator* of a function $f \in \mathcal{H}(V)$, at a vertex $u \in V$, is the vector operator defined by $\nabla_w f(u) = [(df)(u, v_1), \ldots, (df)(u, v_k)]^T$, $\forall(u, v_i) \in E$. The $\mathcal{L}_2$-norm of this vector represents the *local variation* of the function f at a vertex of the graph. It is defined by $\|\nabla_w f(u)\| = \sqrt{\sum_{v \sim u} w(u, v)(f(v) - f(u))^2}$. Let $p \in (0, +\infty)$ be a real number. The *weighted p-Laplace operator* of a function $f \in \mathcal{H}(V)$, noted $\Delta_w^p : \mathcal{H}(V) \to \mathcal{H}(V)$, is defined by [14]:

$$\Delta_w^p f(u) = \frac{1}{2} \sum_{v \sim u} \gamma_w^f(u, v)(f(u) - f(v)), \tag{1}$$

with

$$\gamma_{w,p}^f(u, v) = w(u, v)(||\nabla_w f(v)||^{p-2} + ||\nabla_w f(u)||^{p-2}). \tag{2}$$

The p-Laplace operator is nonlinear except for $p = 2$. In this latter case, it corresponds to the *combinatorial graph Laplacian* which is one of the classical second order operators defined in the context of spectral graph theory [17]. In this paper, we only consider the case where $p = 2$.

3.3. Discrete regularization framework

To regularize a function $f^0 \in \mathcal{H}(V)$ using the p-Laplacian (1), we consider the following general variational problem on graphs:

$$\min_{f \in \mathcal{H}(V)} \left\{ E_{w,p}(f, f^0, \lambda) = R_{w,p}(f) + \frac{\lambda}{2} \|f - f^0\|^2 \right\}, \tag{3}$$

The intuition behind regularization is to provide a smoother version of an initial function (with the regularizer term) while keeping it close to the initial function (with the fitting term). The first term, $R_{w,p}(f)$, is the regularizer and is defined as the discrete Dirichlet form of the function $f \in \mathcal{H}(V)$: $R_{w,p}(f) = \frac{1}{2} \sum_{u \in V} ||\nabla_w f(u)||^p$. The second term is the fitting term. $\lambda \geq 0$ is a fidelity parameter called the Lagrange multiplier which specifies the trade-off between the two competing terms. Both terms of $E_{w,p}(f, f^0, \lambda)$ in (3) are strictly convex function of f [18]. By standard argument in convex analysis, this optimization problem has a unique solution which satisfies, for all $u \in V$ [14]:

$$\frac{\partial}{\partial f(u)} E_w(f, f^0, \lambda) = \Delta_w^p f(u) + \lambda(f(u) - f^0(u)) = 0. \tag{4}$$

Eq. (4) can be interpreted as the discrete analogue of the Euler–Lagrange equation. Using the p-Laplacian formulation (1) in (4), the optimization problem solution can be rewritten as the solution of a system of equations. To approximate the solution of the minimization (3), we can linearize this system of equations and use the Gauss–Jacobi method to obtain the following iterative algorithm for $p = 2$ [14]:

$$\begin{cases} f^{(0)}(u) &= f^0(u) \\ f^{(t+1)}(u) &= \dfrac{\lambda f^0(u) + \sum\limits_{v \sim u} w(u, v) f^{(t)}(v)}{\lambda + \sum\limits_{v \sim u} w(u, v)}, \quad \forall u \in V. \end{cases} \tag{5}$$

This corresponds to Tikhonov regularization on weighted graphs. Other classical filters can be recovered with specific parameters, e.g., with $\lambda = 0$ and $w(u, v) = 1$, $\forall (u, v) \in E$, a Gaussian smoothing is obtained. Our regularization framework enables to smooth the image while preserving its important structures (with the use of the weight function) and avoiding to be too far from the original image (with the fitting-term).

Fig. 3 presents a regularization result on an image. The image is globally smoothed while preserving its main elements unlike a traditional Gaussian smoothing.

3.4. Discrete label regularization

The previous discrete regularization can also be adapted to perform image segmentation by discrete label regularization [15]. Numerous automatic segmentation schemes have been proposed in literature and they have shown their efficiency. Meanwhile, recent interactive image segmentation approaches have been proposed. They reformulate image segmentation into label propagation strategies [19–23]. The previously presented discrete regularization framework can be naturally adapted to address this learning problem for segmentation by label regularization. To accommodate the previous discrete regularization framework to label regularization, we must reformulate the problem. The label regularization of a set of vertices V composed of labeled and unlabeled data consists in grouping the whole set V into k classes with k, the number of classes (known beforehand). The aim is therefore to estimate the unlabeled data from labeled ones.

Let $C = \{c_i\}_{i=1,...,k}$ be the set of initial *labeled* vertices and let $V \setminus C$ be the initial *unlabeled* vertices. This situation can be modeled by considering k initial label functions (one per class) $f_i^0 : V \to \mathbb{Z}$; with $i = 1, ..., k$. For a given vertex $u \in V$, if u is initially labeled then

$$f_i^0(u) = \begin{cases} +1, & \text{if } i \in c_i \\ -1, & \text{otherwise.} \end{cases} \tag{6}$$

If u is initially unlabeled (i.e., $u \in V \setminus C$) then $f_i^0(u) = 0$. Then, the vertex labeling is performed by k regularization processes estimating membership functions $f_i : V \to \mathbb{R}$ for each class i. Using the previously proposed discrete regularization framework, this is formalized as follows:

$$\min_{f_i \in \mathcal{H}(V)} \left\{ R_{w,p}(f_i) + \frac{\lambda}{2} \|f_i - f_i^0\|^2 \right\}, \tag{7}$$

We use the discrete diffusion process (5) to compute each minimization. At the end of the label propagation process, the class membership probabilities of each vertex to a given class can be estimated. Then, the final classification can be obtained for a given vertex $u \in V$ by the following formulation. For all $i \in 1, ..., k$, the label assigned to a vertex u is:

$$\underset{i}{\text{argmax}} \left\{ \frac{f_i(u)}{\sum\limits_i f_i(u)} \right\} \tag{8}$$

The parameter λ is used to tune the dependance to the initial labels. When $\lambda > 0$, the label regularization is highly oriented by initial labels. When the $\lambda = 0$, the algorithm has the ability to modify the initial labels. Fig. 4 shows an example of label regularization with different values of λ. One can see that the label regularization has enabled to refine the boundaries. The less the value of λ the more the label change and the more the boundaries are smoothed.

4. Multi-resolution segmentation approach

In this section, we show how the previous regularization framework on graphs can be used within a multi-resolution segmentation process for mitotic cell extraction.

4.1. Principle

As it has been previously pointed out, a multi-resolution segmentation process is a natural approach to analyze whole slide images [13,24]. Indeed, we have described in Section 2.1 the whole slide image analysis visual process performed by pathologists. This process is a multi-resolution process: a pathologist determines regions of interest at low resolution while cellular classification is performed at high resolution.

Our proposed multi-resolution segmentation process is based on a top-down segmentation [24] that mimics the interpretation process performed by pathologists (see Fig. 2).

According to Fig. 2, our multi-resolution approach considers the images at four increasing resolution levels. First level discriminates the background of the slide from the tissue. Second level discriminates, inside the previously extracted tissue region, the normal surrounding tissue from the lesion. Third level discriminates, inside the previously extracted lesion region, the tumorous cells groups from the stroma. Fourth level discriminates, inside
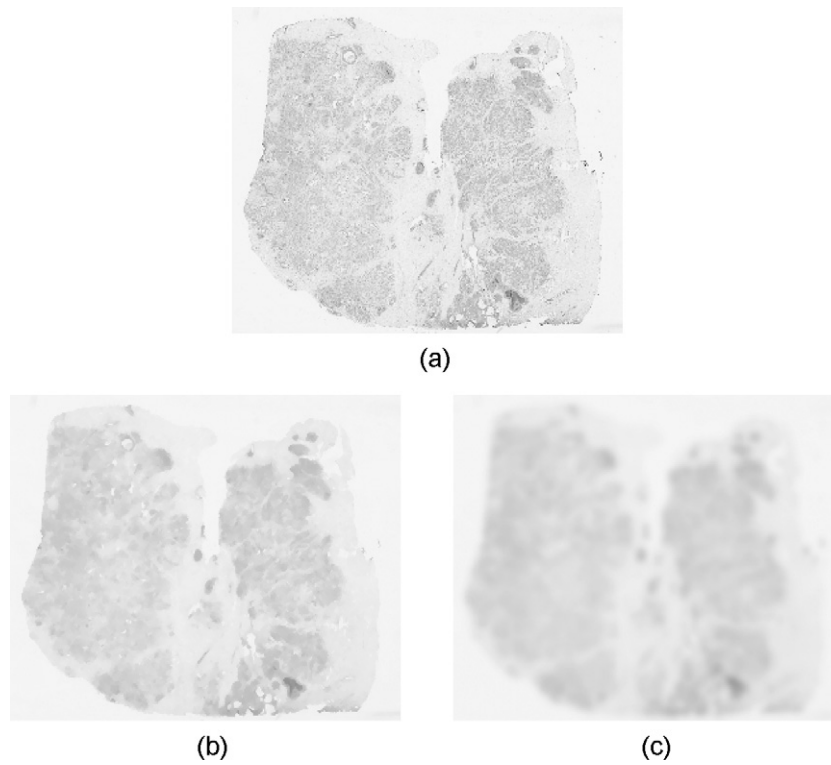
Fig. 3. Illustration of the regularization process after 10 iterations. (a) Initial image, (b) regularized image ($p = 2$, $\lambda = 0.01$, $w(u, v)$ is a Gaussian kernel with $\sigma = 20$), (c) traditional Gaussian filtering ($p = 2$, $\lambda = 0$ and $w(u, v) = 1$).
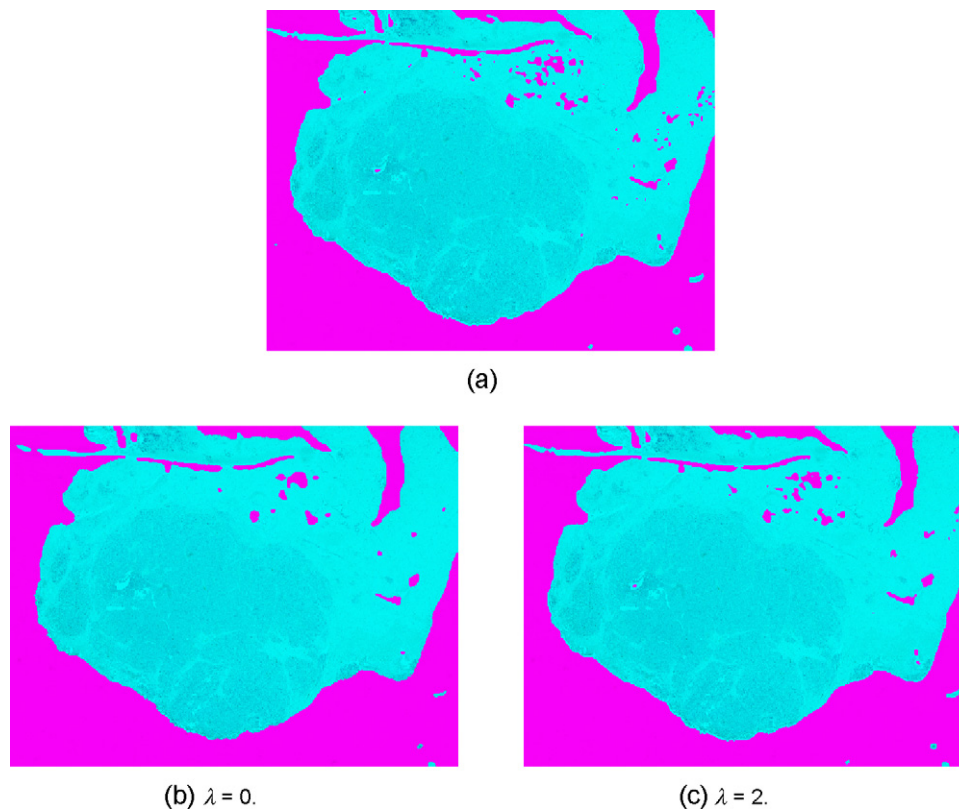

Fig. 4. Illustration of the label regularization process. (a) presents the initial image with labels superimposed, (b)–(c) present the initial image with regularized labels superimposed (with $\lambda = 0$. and $\lambda = 2$.).

the previously extracted tumorous cells groups, the tumorous cells from the mitotic cells. Figs. 10 and 11 provide results for several whole slide images.

At each resolution level, the differentiation between the different components (inside specific regions) is performed by: discrete regularization, unsupervised 2-means clustering, and label regularization in a narrow band around the boundaries to refine the boundaries of the extracted components. We detail all these steps in the following.

4.2. The whole multi-resolution segmentation

The whole segmentation strategy is summarized by Algorithm 1. The resolution level of processing is denoted by i. Level 1 is the coarsest resolution and level 4 is the finest. Since images are tiled, a tile t of an image at the i th level is denoted by $I_{i,t}$. If a superscript is added to $I_{i,t}$, this denotes the result of the processing of a tile. At a given level i, the processing runs into three steps:

Step 1: The histogram of the image at the i th resolution is constructed from regularized tiles in specific regions of interest. Regions of interest are determined from the previous level segmentation.

Step 2: Once the histogram of the image at the i th resolution has been built, a 2-means clustering is performed on this histogram and two cluster centers are obtained.

Step 3: Each tile of the image at the i th resolution is partitioned into two classes according to the cluster centers obtained at step 2. This partition is spatially refined on the level of its boundaries.

Algorithm 1. Multi-resolution WSI segmentation

```
1:  for Level i = 1 to 4 do
2:      {STEP 1}
3:      InitializeHistogram H_i of level i
4:      for Each tile t of level i do
5:          I^p_{i,t} = ReplicateClustering(I^r_{i-1,t}) when i > 1
6:          if i=1 or I^p_{i,t} contains pixels of label i then
7:              I^s_{i,t} = Regularization(I_{i,t})
8:              Update H_i with pixels of I^s_{i,t} (of label i in I^p_{i,t} when i > 1)
9:          end if
10:     end for
11:     {STEP 2}
12:     {C^1_i, C^2_i} = Compute − 2 − MeansClustering(H_i)
13:     {STEP 3}
14:     for Each tile t of level i do
15:         if I^p_{i,t} contains pixels of label i then
16:             I^c_{i,t} = Apply − 2 − MeansClustering(I^s_{i,t}, C^1_i, C^2_i)
17:             I^r_{i,t} = SpatialClusteringRefinement(I^c_{i,t}, I_{i,t})
18:         else
19:             I^r_{i,t} = I^p_{i,t}
20:         end if
21:     end for
22: end for
```

4.3. First step: histogram construction

As a first step, we construct a color histogram of the image at the i th resolution level. Since the images are tiled, we run through all the tiles to construct the histogram incrementally (Update in Algorithm 1). We mention now how this histogram is constructed.

First, this histogram is not build directly from the raw tiles but from regularized version of the tiles (Regularization in Algorithm 1). The regularization of each tile is performed by discrete graph regularization with the image modeled as a weighted 8-adjacency grid-graph with $\lambda = 0.01$. The effect of the regularization process was previously illustrated in Fig. 3. The aim of the reg-

ularization step is to simplify the color distribution of colors in their feature space (i.e., in the histogram H_i) for a further easier clustering in step 2. Fig. 5 illustrates this. Fig. 5a presents the distribution of the colors in the *RGB* color space for an image at the first level of resolution (i.e., the colors of Fig. 3a), and Fig. 5b shows the distribution of colors after regularization (i.e., the colors of Fig. 3b). One can see that the color outliers have disappeared in the simplified color distribution: this will further facilitate the task of the step 2 in Algorithm 1 performing an unsupervised 2-means clustering.

Second, the histogram is constructed only from specific regions of interest except for the first level. At the first level (i.e., $i = 1$) the histogram is constructed from all the tiles. This histogram will be used in steps 2 and 3 to obtain a segmentation $I^r_{1,t}$ between tissue (label 2) and background (label 1) for each tile $I_{1,t}$ of the first level. At the second level of resolution, the segmentation obtained at the previous level is replicated on each tile $I_{2,t}$ according to the increase of resolution (ReplicateClustering in Algorithm 1). Then, the histogram is constructed only inside regions that were considered as tissue at the previous level of resolution. As a consequence, the histogram considers only pixels that had the label 2 in the segmentation obtained at the previous resolution (expressed by the tests on the pixel labels in the first step of Algorithm 1). This principle is also applied for the next levels. To illustrate this, Fig. 6a presents the segmentation obtained at the first level of resolution. Fig. 6a shows the tiles that are retained for the construction of the histogram at the second level of resolution: tiles that do not contain pixels of label 2 (i.e., the tissue depicted in cyan) are not considered. Fig. 6c and d illustrates again this principle but for the third level of resolution: tiles that do not contain pixels of label 3 (i.e., the lesion depicted in yellow) are not considered.

4.4. Second step: histogram 2-means clustering

Once the histogram H_i is obtained at a given resolution level i, this histogram is clustered into two classes by using a k-means clustering with $k = 2$. The advantages of the k-means algorithm are its simplicity and speed which allows it to run on large datasets. However, this algorithm is not robust to the initialization of the centers of clusters. So, we use a robust version of the k-means algorithm that is not sensitive to initialization [25] and considers an histogram to perform the clustering. This clustering provides us the centers $\{C^1_i, C^2_i\}$ of the two extracted classes.

We mention now why we prefer to perform the 2-means clustering on the histogram of the considered tiles at one level of resolution i. If we had performed naively a 2-means clustering on each tile, we would have obtained strong problems at tiles' boundaries since the content of one sole tile is not necessarily representative of the global information. For example, the tile can contain only one type of structure we want to extract but if this tile is treated as a sole, two clusters will be extracted even if it has not to be the case. Fig. 7a–c illustrates this for the segmentation at the first resolution level. One can easily see that incoherent segmentation is obtained for the adjacent tiles. This illustrates the advantage of performing the clustering on the histogram rather than tile by tile (as this classically performed on whole slide image e.g., in [13]): this ensures that the clustering is coherent on the whole i th image.

Finally, we detail the color feature space considered for the clustering at each resolution level. For levels 1–3, the clustering is performed on *RGB* feature vectors. For level 4, dedicated to mitosis extraction, the clustering is performed on a specific feature scalar, the Red-Cyan difference, that proved its robustness in previous works [26]. Indeed, mitosis are visually recognizable by a color close to the brown that can be easily stressed by chromatic information with the Red-Cyan difference ($2R - G - B$) (see Fig. 8).
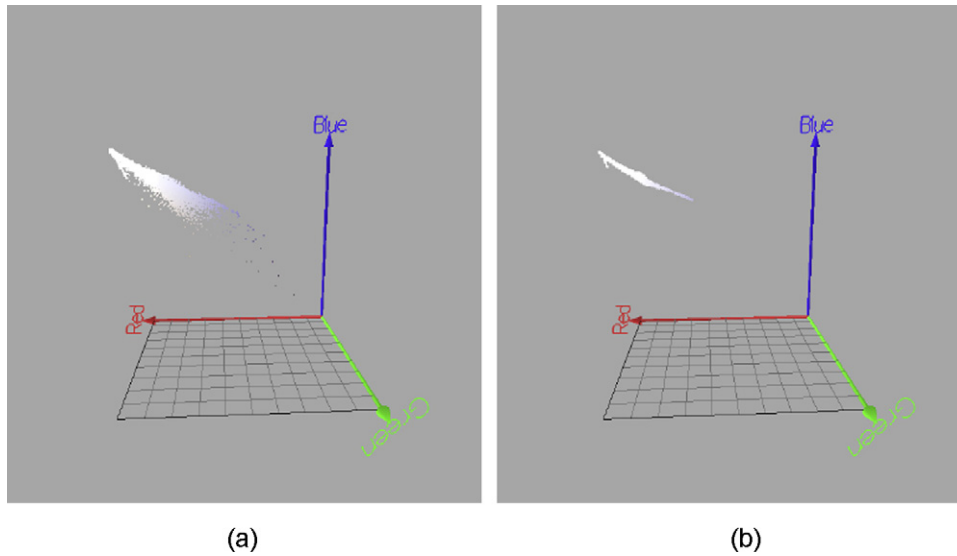
Fig. 5. The distribution of colors in the *RGB* color space before (a) and after (b) image regularization for the images of Fig. 3.

4.5. Third step: partitioning and spatial refinement

From the cluster centers $\{C_i^1, C_i^2\}$ extracted at one resolution level i, we run through the tiles of the ith image. For each considered tile, pixels are affected to their closest cluster center (`Apply-2-MeansClustering` in Algorithm 1). For unconsidered tiles, the labels are replicated from tiles of the previous level. The clustering being performed in the color feature space for considered tiles, no spatial information is taken into account and the obtained segmentation is not accurate around boundaries (neither for pixels labels that have been replicated from the previous level). To avoid this effect, we use our discrete label regularization described in Section 3.4 to modify the clustering results by taking into account spatial information in the image domain. Therefore, we adapted our label regularization to have its range limited to the boundaries of the extracted elements (`SpatialClusteringRefinement` in Algorithm 1).

Let $V^i = \{u_1^i, \ldots, u_N^i\}$ denote the set of vertices of a grid-graph $G^i = (V^i, E^i, w)$ associated to a tile at a given ith resolution level.
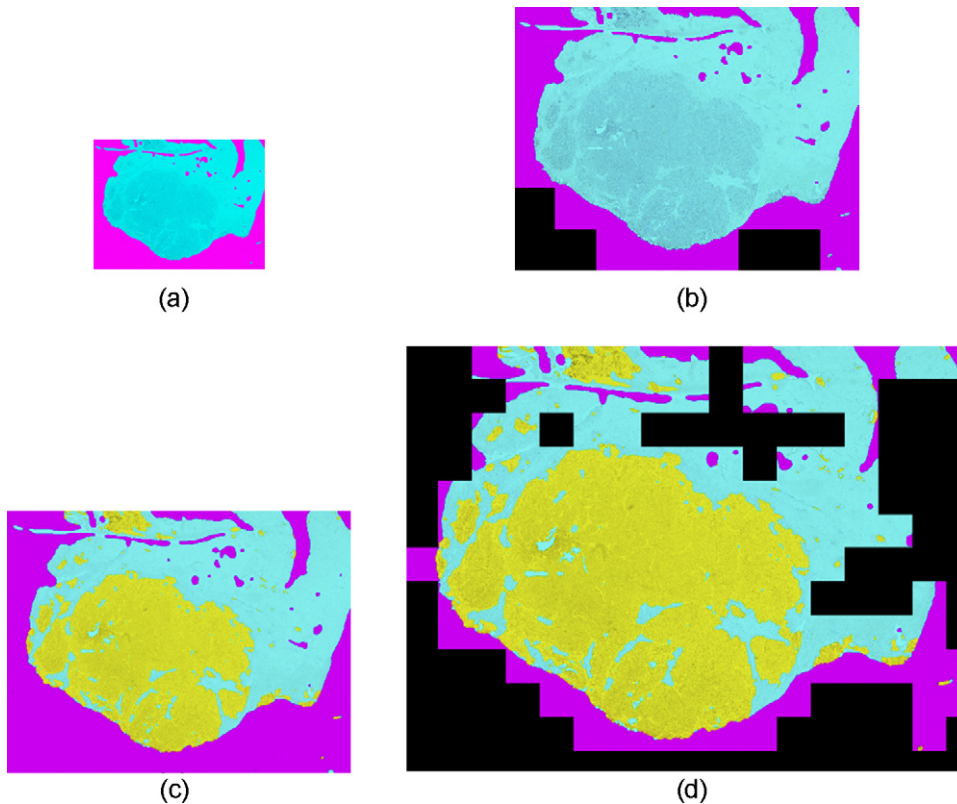

Fig. 6. Illustration of the retained regions for processing: (a) and (c) present the segmentation obtained at the first and second resolution levels, (b) and (d) show the tiles considered for the segmentation at the second and third resolution level: black areas correspond to unconsidered tiles where pixel label replication is used.
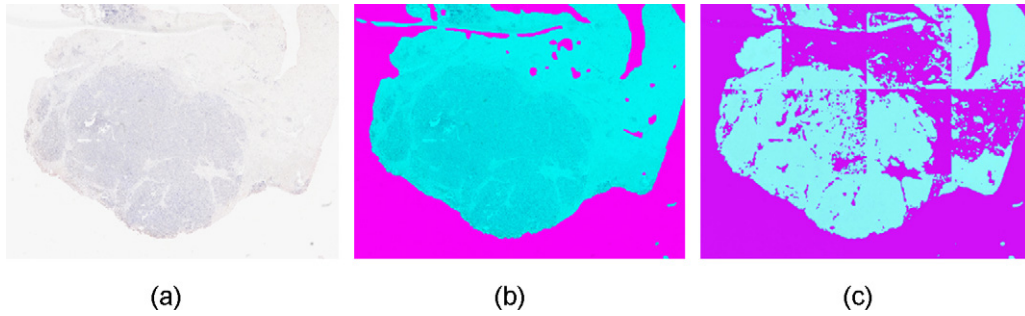
Fig. 7. Illustration of the inaccuracy of tile by tile clustering at the first level of resolution. (a) The tiled image of the first level. (b) Accurate global processing. (c) Inaccurate tile by tile processing: artificial divisions appear.

Each vertex is associated with a cluster label $l : V \rightarrow \mathbb{Z}$ previously obtained by 2-means clustering or a replication of labels at lower resolution. The set of vertices associated to one cluster j is: $V_j^i = \{u \in V^i : l(u) = j\}$ where $j = 1, \ldots, C$ with C the final number of classes.

The aim of the clustering spatial refinement is to modify the labels assigned to vertices in order to have a clustering that is better delineated along its boundaries. Therefore, we use the discrete label regularization formulation previously presented in Section 3.4. In this case, all the vertices are initially labeled and their label can be modified by the regularization process (5) with λ set to zero.

Moreover, since the spatial refinement has to be performed only around the boundaries of objects, we consider a specific grid-graph that is a subset of the whole grid-graph. The set of vertices that corresponds to the boundaries between two different clusters at i th resolution level is defined by:

$$\partial V^i = \{u \in V^i : \exists v \in V^i \quad \text{with} \quad (u, v) \in E^i \text{ and } l(u) \neq l(v)\}.$$

The set of vertices that belongs to a narrow band of size $2\delta + 1$ around the set ∂V^i is defined by:

$$\partial^+ V^i = \{u \in V^i : \exists v \in \partial V^i \quad \text{with} \quad d(u, v) \leq \delta\}$$

where $d(u, v)$ is the distance of the path

$$\{u = v_1, v_2, \ldots, v_n = v\}$$

with $(v_j, v_{j+1}) \in E^i, \forall i$. The set of edges E^{i+} is defined as the subset of edges in E^i that connects two vertices of $\partial^+ V^i$:

$$E^{i+} = \{(u, v) \in E^i : u, v \in \partial^+ V^i\}.$$

The clustering spatial refinement is then accomplished by k regularization processes on the graph $G^{i+} = (\partial^+ V^i, E^{i+}, w)$ as described in Section 3.4. The clustering spatial refinement is illustrated in Fig. 9. From an initial segmentation (Fig. 9a), a narrow band is considered around the boundaries (Fig. 9b) and the labels are modified by discrete regularization (Fig. 9c) to obtain more accurate boundaries (Figs. 10 and 11).

5. Visualization of mitotic figures

Once all the mitosis have been extracted at the highest resolution using our top-down multi-resolution graph-based extraction algorithm, the pathologist has to visualize them to establish by himself the mitotic score. Indeed, in the Elston–Ellis criterion, the
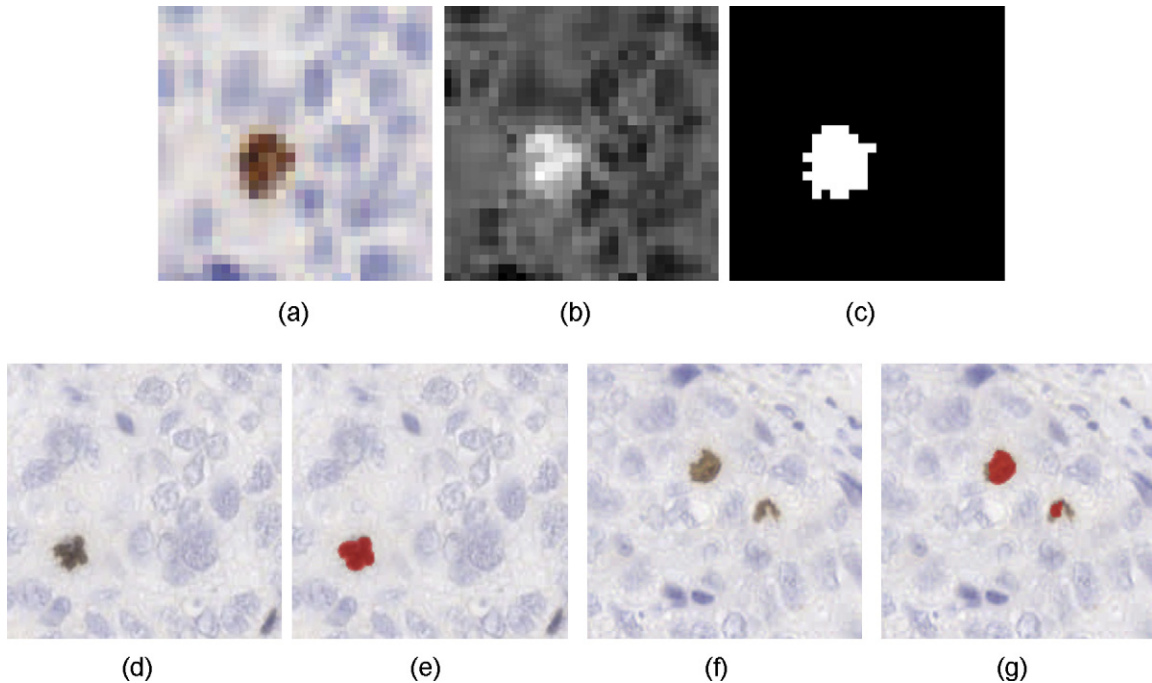

Fig. 8. Illustration of mitotic figures extraction. (a) Initial mitosis. (b) Red-Cyan difference transformation. (c) 2-Means clustering of (b). (d)–(g) show two examples of mitosis detection with the initial image and the image with detected mitosis superimposed in red. (For interpretation of the references to color in this figure legend, the reader is referred to the web version of this article.)
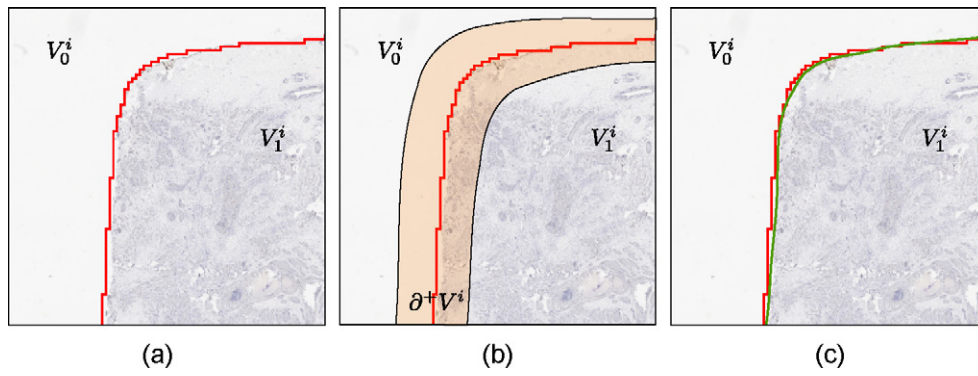
Fig. 9. Illustration of the clustering spatial refinement of a tile. (a) A segmentation obtained for a tile by `Apply-2-MeansClustering` in Algorithm 1. (b) Superimposed narrow band of (a), (c) clustering spatial refinement of (b) with the original boundary of (a). See the electronic version of the paper for a better visualization.
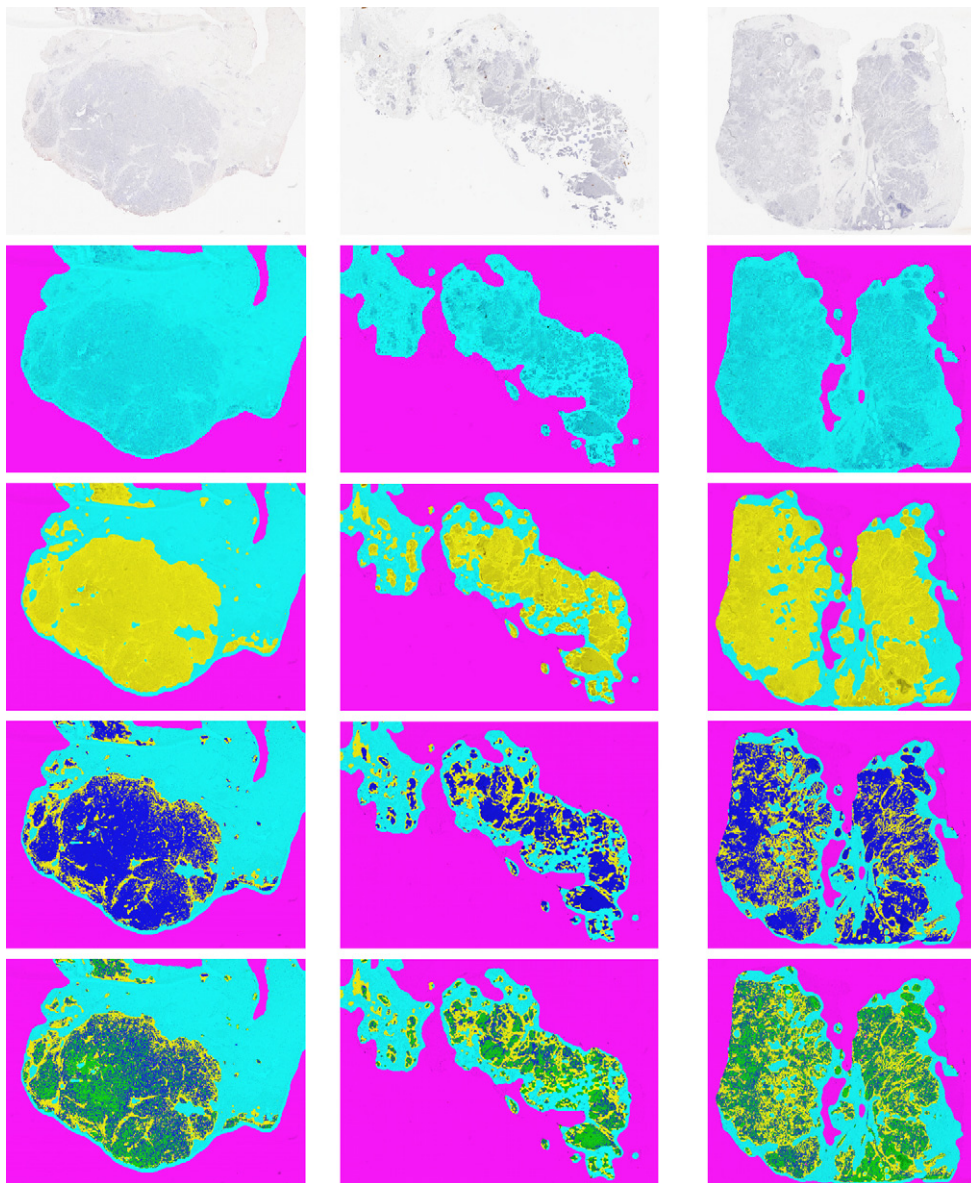

Fig. 10. Illustration of the multi-resolution clustering process. First row: initial images. Second row: first resolution segmentation results (background in pink, tissue in cyan). Third row: second resolution segmentation results (lesion in yellow). Fourth row: third resolution segmentation results (tumorous cells groups in dark blue, stroma in yellow). Fifth row: fourth resolution segmentation results (tumorous cells in green and mitotic figures in red). (For interpretation of the references to color in this figure legend, the reader is referred to the web version of this article.)
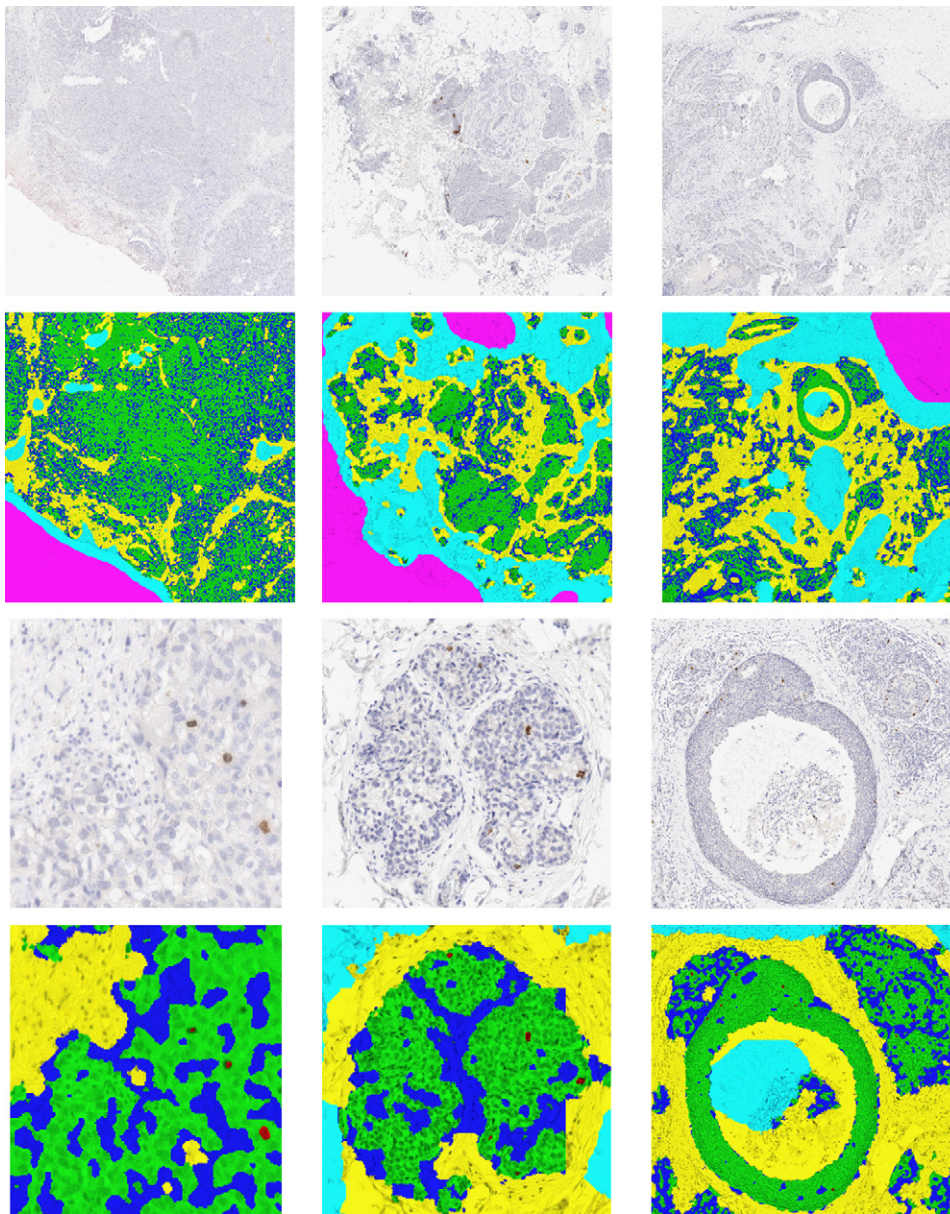
Fig. 11. Detailed illustrations of the multi-resolution clustering process on cropped images. First row: cropped images at the third resolution level. Second row: cropped segmentation results at the third resolution for images of the first row. Third row: cropped images at the fourth resolution level. Fourth row: cropped segmentation results at the fourth resolution for images of the third row. Colors in the segmentation results correspond to: pink for background, tissue in cyan, stroma in yellow, tumorous cells groups in dark blue, tomorous cells in green, mitotic figures in red. (For interpretation of the references to color in this figure legend, the reader is referred to the web version of this article.)

mitotic count is established only on 10 consecutive high power fields in the most mitotic area. These zones have to be chosen by the pathologist. As a consequence, we do not compute directly a mitotic score but help pathologists in doing it. To do so, we provide two visualization tools for pathologists.

5.1. Mitosis distribution visualization

The first one enables the pathologist to evaluate the global repartition of detection mitosis on the whole slide. This visualization tool is necessary to help the pathologist in choosing the areas for establishing its mitotic count. This visual information is provided by superimposing a graph on the whole slide image. The graph is constructed as follows. Each detected mitosis is represented by a vertex of the graph. A Voronoi map is computed on the vertices coordinates and the associated Delaunay graph is obtained. This

enables the pathologist to evaluate zones on the whole slide image where the mitotic activity is important by the superposition of the Voronoi distance map on the whole slide image (Fig. 12). Using this visualization tool, the pathologist can choose areas on the whole slide and obtain a mitotic count for the Elston–Ellis criterion.

5.2. Mitosis phases visualization

The second visualization tool enables the pathologist to see the extracted mitosis altogether on a single 3D projection to appreciate their aspect (e.g., to differentiate the different mitotic phases: prophase, metaphase, anaphase). To do this, each mitosis is described by a Locally Binary Pattern (LBP) histogram [27,28] in the HSL color space. This histogram is used as an input for non-linear dimensionality reduction by Laplacian Eigenmaps [29] with distances between histograms expressed by the Chi square statis-
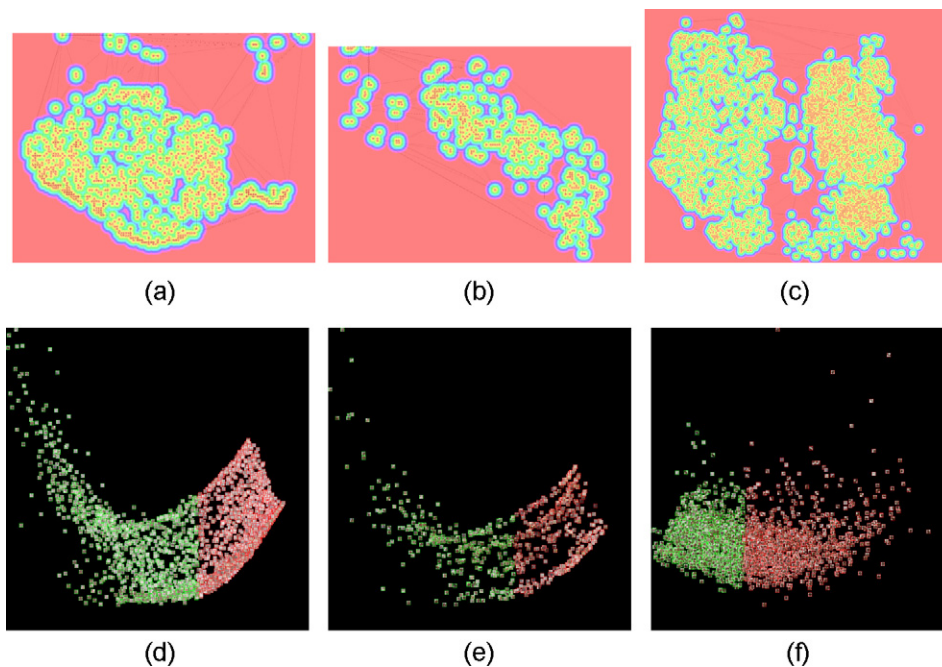
Fig. 12. Illustration of visualization tools of extracted mitotic figures. (a)–(c): Distance maps and Delaunay graphs of the mitosis distribution. (d)–(f): Visualization of extracted mitotic figures by dimensionality reduction for the mitosis of (a)–(c) (see electronic version of the paper for better visualization).

tic. Once the dimensionality reduction has been performed, the pathologist can visualize simultaneously all the mitotic figures of a whole slide image in the form of a 3D projection where each mitosis is projected at coordinates defined by the nonlinear dimensionality reduction. In this projection, mitosis of similar texture will be grouped together. With this tool, the pathologist can estimate the number of mitosis in each mitotic phase. If the pathologist needs it, the set of mitosis can be partitioned into two sets with a normalized cut criterion [30]. This enables to obtain two sets of mitosis with low texture information (prophase and metaphase) or high texture information (anaphase). These two sets are shown by coloring the bounding box of the mitosis in the projection (Fig. 12g–i). Identifying the different mitotic phases is useful for evaluating their relative frequency. This can provide information on the length of each phase and account for the kinetics of proliferation. This information is not a criterion in the Elston–Ellis grading but this provides an information that is useful to evaluate the evolution in time of a tumor.

6. Evaluation results

In terms of processing time, our algorithm takes at most 30 min (on a Intel Core is 2.4 GHz with 4 Gb RAM) to process a multi-resolution pyramidal image having $45,000 \times 38,000$ pixels at its finest resolution. This processing time is obtained without any parallelization that can be easily integrated within our algorithm since the images are tiled. Regarding memory usage, our algorithm manipulates simultaneously a 3D-histogram for the clustering (of size $256^3 \sim 48$ Mb), and several instances of a tile of size 256×256 (for the original, the regularized image, the clustered one and the spatially refined one) giving a size of ~ 2 Mb. The whole memory manipulated by our algorithm during the processing is therefore of ~ 50 Mb which is really low.

The evaluation of the accuracy of an image processing on whole slide images is very difficult. Indeed, whole slide images being very large, a quantitative quality control becomes very complex to achieve and almost impossible regarding the thousands of elements to evaluate. To cope with this problem, sampling methods

of stereology [31] can be used to limit the tedious quality control work. On whole slide images, a stereological-based quality control consists in superimposing a grid on the whole slide image at full-resolution and evaluating the quality of the processing only in the areas that overlap the grid. Two sorts of grids can be used [32]: a grid of points allows to compute fractions of surface, a grid of frames allows to compute densities. We have considered both these types of grid for evaluation of our segmentation scheme (Fig. 2). Eight whole slide images of different cancer grades have been considered for the evaluation by one pathologist. After a first qualitative visual evaluation, pathologists agreed that the segmentation results were very good for levels 1 (tissue versus background) and 2 (lesion versus normal surrounding tissue) and do not need to be quantitatively evaluated. Therefore, we focused only on the evaluation of the segmentation for level 3 (tumorous cells groups versus stroma) and level 4 (mitotic figures versus other cells). For the evaluation of the segmentation performed at level 3, a point grid is used to estimate the fraction of surface of correctly detected tumorous cells groups. For the evaluation of the segmentation performed at level 4, a frame grid is used to evaluate the density of correctly detected mitosis. Fig. 13 shows the principle of stereological evaluation with point or frame grids using the Stereology Software module of Adcis and Aperio® Technologies, Inc.

6.1. Evaluation of tumorous cells groups detection

As previously explained, a point counting stereological evaluation is conducted to quantify the tumorous cells groups detection. When a pathologist performs this evaluation, for each point of the grid, he specifies if the structure detected at the coordinates of this point corresponds to true/false positive/negative. To better understand the results of the stereological evaluation, two measures are used. Sensitivity and specificity are statistical measures of the performance of a binary classification test. Sensitivity measures the proportion of actual positives which are correctly identified as such. Specificity measures the proportion of negatives which are correctly identified. Given *TP* the number of true positive, *FP* the number of false positive, *TN* the number of true negative, and *FN*

(a) A grid of points superimposed on a whole slide image.

(b) Checked points that are in tumorous cells groups.

(c) A grid of frames superimposed on a whole slide image.
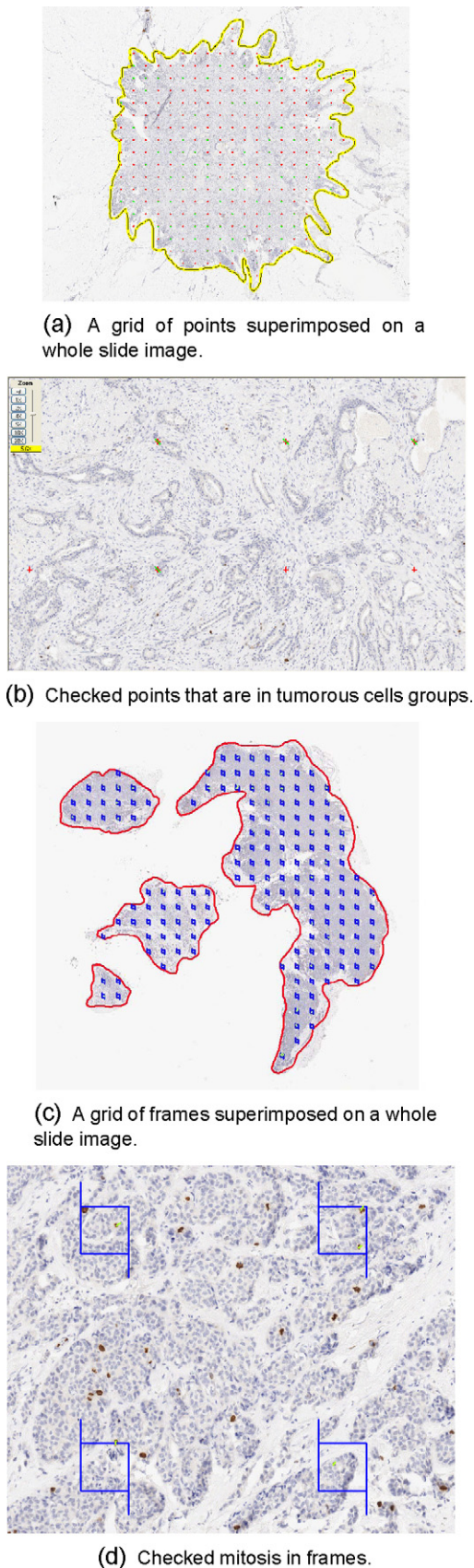

(d) Checked mitosis in frames.

Fig. 13. Illustration of the stereological segmentation quality evaluation for grids of points or frames.
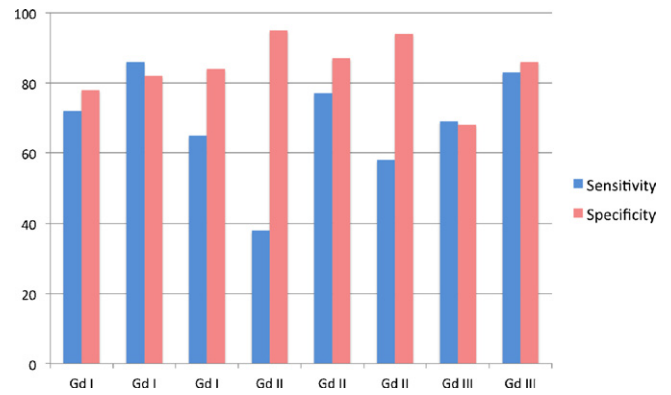

Fig. 14. Sensitivity and specificity for evaluation of the segmentation of tumorous cells groups according to grades estimated by pathologists.

the number of false negative, sensitivity is defined as $TP/(TP+FN)$ and specificity is $TN/(TN+FP)$. With these values, sensitivity and specificity measures are obtained for the detection of tumorous cells groups (see Fig. 14). As one can see, our proposed segmentation process has a good sensitivity (>70%) for Grade 1 and Grade 3. Sensitivity is around 60% for the Grade 2. Whatever the grades, specificity is around 80%. We can conclude that our method work reasonably well for Grades 1 and 3 but has to be improved for Grade 2 that can exhibit very different tissue organization. For example, the first case of Grade 2 in our database is an invasive tubular tumor that produces aligned tumorous cells, while our method is designed to detect massive tumorous groups of cells.

6.2. Evaluation of mitotic figures extraction

A frame counting stereological evaluation is conducted to quantify the extraction of mitotic cells. However due to the sparseness and low number of mitosis for Grade 1 and 2, this type of stereological evaluation is not adapted (results will not be statistically significative) and we have performed the evaluation only for Grade 3 that exhibits much more mitosis. It appears that our method is very specific and does not make any false positive. However it can miss some mitosis leading to an average detection rate of 70%. To better understand the reasons for our method to miss the extraction of some mitosis, pathologists have evaluated these cases. First, it appears that mitosis that are in early prophase are not detected due to the fact that immunohistochemical staining is low. These errors can be easily corrected by performing a less strong regularization before clustering. Second, with our multi-resolution algorithm, we try to detect mitosis only in regions that were previously extracted at level 3 as containing tumorous cells groups. However, as we have seen in the previous evaluation of tumorous cells groups detection, some regions that contain tumorous cells are not accurately detected and therefore no mitosis extraction is performed in these areas. These errors of detection can be corrected only by correcting the detection of tumorous cells groups.

To conclude these evaluation results, the whole multi-resolution works reasonably well. Three levels of segmentation can be considered as good: level 1 (tissue versus background), level 2 (lesion versus normal surrounding tissue) and level 4 (mitotic figures versus other cells). However the segmentation obtained in level 3 (tumorous cells groups versus stroma) has be enhanced to better detect zones containing tumorous cells groups especially for Grade 2. This will be achieved in future works by integrating texture information in addition to color features.

7. Conclusion

In this paper, a multi-resolution image analysis strategy for automatic enumeration of mitotic figures on whole slide images is proposed. The whole classification process begins with the lowest resolution image and moves to higher resolution into regions of interest gradually identified. Graph-based regularization provides a unified formalism for both image simplification and spatial boundary refinement. Contrary to methods that can be found in literature, our method is completely unsupervised and has the advantage of reducing the amount of data to be processed at each resolution level by selecting regions of interest.

We also proposed two methods for the visualization of mitotic figures. The first method allows to visualize the distribution of mitosis on the tissue samples. The second method groups mitosis according to texture parameters.

Evaluation results have shown that our method is globally efficient, but some improvement is needed for the detection of tumorous cells groups, especially for tumors of Grade 2. Future works will concern the integration of texture information for the enhancement of tumorous cell groups as well as the automation of the other scores of the Elston–Ellis grading systems.

Acknowledgments

References

[1] Tavassoli F, Devilee P. Pathology and genetics tumours of the breast and female genital organ. International Agency for Research on Cancer Press; 2003.

[2] Gillett CE. Assessment of cellular proliferation by calculation of mitotic index and by immunohistochemistry. In: Metastasis research protocols, volume 57 of methods in molecular medicine. Humana Press; 2001. p. 123–31.

[3] Demir C, Yener B. Automated cancer diagnosis based on histopathological images: a systematic survey. Technical Report, Rensselaer Polytechnic Institute; 2005.

[4] Petushi S, Garcia F, Haber M, Katsinis C, Tozeren A. Large-scale computations on histology images reveal grade-differentiating parameters for breast cancer. BMC Medical Imaging 2006;6:1–11.

[5] Naik S, Doyle S, Agner S, Madabhushi A, Feldman MD, Tomaszewski J. Automated gland and nuclei segmentation for grading of prostate and breast cancer histopathology. In: International symposium on biomedical imaging; 2008. p. 284–7.

[6] Doyle S, Agner S, Madabhushi A, Feldman MD, Tomaszewski J. Automated grading of breast cancer histopathology using spectral clustering with textural and architectural image features. In: International symposium on biomedical imaging; 2008. p. 496–9.

[7] Ruiz A, Kong J, Ujaldon M, Boyer K, Saltz J, Gurcan M. Pathological image segmentation for neuroblasma using the gpu. In: International symposium on biomedical imaging; 2008. p. 296–9.

[8] Doyle S, Madabhushi A, Feldman M, Tomaszeweski J. A boosting cascade for automated detection of prostate cancer from digitized histology. In: International conference on medical image computing and computer assisted intervention; 2006. p. 504–11.

[9] Fuchs TJ, Wild PJ, Moch H, Buhmann JM. Computational pathology analysis of tissue microarrays predicts survival of renal clear cell carcinoma patients. In: International conference on medical image computing and computer assisted intervention, vol. 2; 2008. p. 1–8.

[10] Signolle N, Plancoulaine B, Herlin P, Revenu M. Texture-based multiscale segmentation: Application to stromal compartment characterization on ovarian carcinoma virtual slides. In: International conference on image and signal processing, vol. LNCS 5099; 2008. p. 173–82.

[11] Elston CW, Ellis IO. Pathological prognostic factors in breast cancer. I. The value of histological grade in breast cancer: experience from a large study with long-term follow-up. Histopathology 1991;19:403–10.

[12] Dalle J, Leow W, Racoceanu D, Tutac A, Putti T. Automatic breast cancer grading of histopathological images. In: International conference of the IEEE engineering in medicine and biology society; 2008. p. 3052–5.

[13] Kong J, Sertel O, Shimada H, Boyer K, Saltz J, Gurcan M. Computer-aided evaluation of neuroblastoma on whole-slide histology images: classifying grade of neuroblastic differentiation. Pattern Recognition 2009;42:1080–92.

[14] Elmoataz A, Lézoray O, Bougleux S. Nonlocal discrete regularization an weighted graphs: a framework for image and manifolds processing. IEEE transactions on Image Processing 2008;17:1047–60.

[15] Ta V-T, Lézoray O, Elmoataz A, Schüpp S. Graph-based tools for microscopic cellular image segmentation. Pattern Recognition 2009;42:1113–25.

[16] Diestel R. Graph theory volume 173 of graduate texts in mathematics. Springer-Verlag; 2005.

[17] Chung FR. Spectral graph theory. CBMS Regional Conference Series in Mathematics 1997;92:1–212.

[18] Chan T, Osher S, Shen J. The digital TV filter and nonlinear denoising. IEEE Transactions on Image Processing 2001;10:231–41.

[19] Wang F, Wang J, Zhang C, Shen HC. Semi-supervised classification using linear neighborhood propagation. International Conference on Computer Vision and Pattern Recognition, 1. 2006. p. 160–7.

[20] Grady L. Random walks for image segmentation. IEEE Transactions on Pattern Analysis and Machine Intelligence 2006;28:1768–83.

[21] Sinop AK, Grady L. A seeded image segmentation framework unifying graph cuts and random walker which yields a new algorithm. In: International conference on computer vision; 2007. p. 1–8.

[22] Zhou D, Schölkopf B. Regularization on discrete spaces. In: German association for pattern recognition DAGM, vol. LNCS 3663; 2005. p. 361–8.

[23] Belkin M, Niyogi P, Sindhwani V, Bartlett P. Manifold regularization: a geometric framework for learning from labeled and unlabeled examples. Journal of Machine Learning Research 2006;7:2399–434.

[24] Roullier V, Ta V-T, Lézoray O, Elmoataz A. Graph-based multi-resolution segmentation of histological whole slide images. In: International symposium on biomedical imaging; 2010. p. 153–6.

[25] Kanungo T, Mount D, Netanyahu N, Piatko C, Silverman R, Wu A. An efficient k-means clustering algorithm: Analysis and implementation. IEEE Transactions on Pattern Analysis and Machine Intelligence 2002;24:881–92.

[26] Elie N, Plancoulaine B, Signolle J-P, Herlin P. A simple way of quantifying immunostained cell nuclei on the whole histologic section. Cytometry Part A 2003;56A:37–45.

[27] Ojala T, Pietikäinen M, Harwood D. A comparative study of texture measures with classification based on feature distributions. Pattern Recognition 1996;29:51–9.

[28] Ojala T, Pietikäinen M, Maenpaa T. Multiresolution gray-scale and rotation invariant texture classification with local binary patterns. IEEE Transactions on Pattern Analysis and Machine Intelligence 2002;24:971–87.

[29] Belkin M, Niyogi P. Laplacian eigenmaps for dimensionality reduction and data representation. Neural Computation 2003;15:1373–96.

[30] Shi J, Malik J. Normalized cuts and image segmentation. IEEE Transactions on Pattern Analysis and Machine Intelligence 1997;22:888–905.

[31] Howard C, Reed M. Unbiased stereology three-dimensional measurement in microscopy, 2nd ed. QTP Publications; 2010.

[32] Herlin P, Lay B, Bouchard H, Pezeril H, Lange H, Plancoulaine B. Benefits of stereology for quality control of fully automated virtual slide analysis. In: 10th European congress on telepathology and 4th international congress on virtual microscopy; 2010.